analytical chemistry

pubs.acs.org/ac Article

Plasmonically Calibrated Label-Free Surface-Enhanced Raman Spectroscopy for Improved Multivariate Analysis of Living Cells in Cancer Subtyping and Drug Testing

Wonil Nam, Xiang Ren, Inyoung Kim, Jeannine Strobl, Masoud Agah, and Wei Zhou*

Cite This: *Anal. Chem.* 2021, 93, 4601−4610 Read Online

ACCESS | Metrics & More | Article Recommendations | Supporting Information

ABSTRACT: Plasmonic nanostructure-enabled label-free surface-enhanced Raman spectroscopy (SERS) emerges as a rapid nondestructive molecular fingerprint characterization technique for complex biological samples. However, label-free SERS bioanalysis faces challenges in reliability and reproducibility due to SERS signals' high susceptibility to local optical field variations at plasmonic hotspots, which can bias correlations between the measured spectroscopic features and the actual molecular concentration profiles of complex biochemical matrices. Herein, we report that plasmonically enhanced electronic Raman scattering (ERS) signals from metal nanostructures can serve as a SERS calibration internal standard to improve multivariate analysis of living biological systems. Through side-by-side comparisons with noncalibrated SERS datasets, we demonstrate that the ERS-based SERS calibration can enhance supervised learning classification of label-free living cell SERS spectra in (1) subtyping breast cancer cells with different degrees of malignancy and (2) assessing cancer cells' drug responses at different dosages. Notably, the ERS-based SERS calibration has the advantages of excellent photostability under laser excitation, no spectral interference with biomolecule Raman signatures, and no occupation competition with biomolecules at hotspots. Therefore, we envision that the ERS-based SERS calibration can significantly boost the multivariate analysis performance in label-free SERS measurements of living biological systems and other complex biochemical matrices.

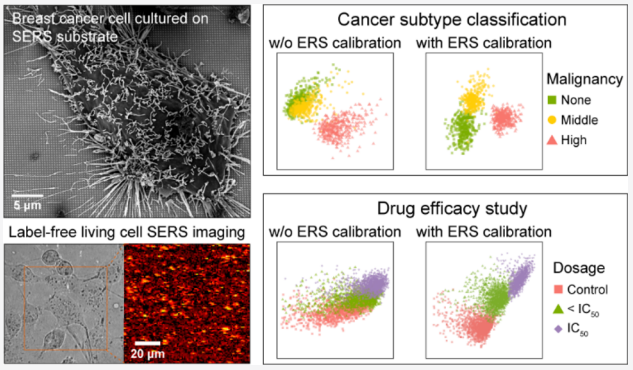

INTRODUCTION

Rapid molecular-level characterization of biological samples is highly desirable for identifying biomarkers related to specific diseases and pathogens, characterizing cellular responses in drug testing, or screening up- or down-regulated pathways but remains challenging in biology and medicine.[1−3] Currently, mass spectrometry and nuclear magnetic resonance spectroscopy are the two gold standard methods for providing quantitative structural information for complex biological samples.[4,5] Nevertheless, these measurements are destructive and time-consuming, suitable for end-point analysis but not for real-time monitoring of dynamic changes in living biological systems. As a promising alternative, surface-enhanced Raman spectroscopy (SERS) has emerged as a label-free, nondestructive, and rapid detection technique to provide vibrational molecular fingerprint information of biological samples without water vibrational interference.[1−3,6−8] Notably, by surface plasmon enhancement of both excitation and inelastic scattering processes for molecules at plasmonic hotspots, the sensitivity of SERS can reach a single-molecule detection limit.[9] Molecular-specific and label-free SERS approaches can allow the detection of specific biomolecules (e.g., metabolites, amino acids, proteins, and nucleic acids) in complex matrices (e.g., food, blood plasma, serum specimens, and body fluids)[10−13] as well as the investigation of dynamic biological processes in living biological systems (e.g., cell cultures, tissues, and animal models).[14−16]

For acquiring intrinsic SERS signatures of living cells, two general forms of SERS-active nanosensors have been developed: colloidal plasmonic nanoparticles and substrate-based plasmonic nanostructures.[3,6] Colloidal plasmonic nanoparticles, by endocytosis, can enable intracellular SERS detection and analysis of the cell death process,[17] cell cycle,[18] and endolysosomal pathways.[19] On the other hand, substrate-based plasmonic nanostructures can provide uniform large-area hotspot arrays for extracellular SERS measurements to classify between cancer and normal cells,[20,21] examine

Received: December 12, 2020
Accepted: February 24, 2021
Published: March 5, 2021

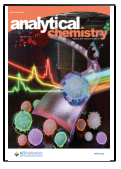

https://dx.doi.org/10.1021/acs.analchem.0c05206
Anal. Chem. 2021, 93, 4601−4610

membrane dynamics with electroporation,[22] and monitor neural stem cell differentiation.[23] Since label-free SERS spectra of living cells typically consist of highly overlapped spectroscopic features from various biomolecules in hotspot ensembles within the laser beam area, multivariate analysis of such high dimensional data is required to extract biologically meaningful knowledge.[3,6,24] Unsupervised learning approaches, such as principal component analysis (PCA), can evaluate spectroscopic features' intrinsic relationships between sample groups and reduce data dimensionality with preserved key variances.[25] Nevertheless, unsupervised learning algorithms are descriptive and thus necessitate further interpretation. Therefore, for interpreting high dimensional SERS spectra of living cells between different types/subtypes or disease/drug states, it is crucial to exploit supervised learning methods and perform multivariate mapping with trained models. Popular supervised learning algorithms for multivariate SERS bioanalysis include linear discriminant analysis (LDA), partial least-squares discriminant analysis (PLS-DA), support vector machines (SVM), and artificial neural networks (ANN).[24,26]

Despite significant advances, label-free SERS analysis of living cells still faces challenges in reliability and reproducibility mainly because SERS signals are incredibly susceptible to local optical field variations at plasmonic hotspots. Spatial variations of SERS signals among different plasmonic hotspots can occur due to variations in nanoscale geometries, the local refractive index (RI) of different intracellular and extracellular components, or optical focusing conditions.[27] Temporal variations of SERS signals can occur because of excitation laser power fluctuations or dynamic cellular perturbations to plasmonic hotspots. Such spatial or temporal variations in SERS signals can mislead interpretation of the actual biomolecule concentrations at hotspots and bias living cell SERS analysis. A promising method for calibrating SERS signals is to generate internal standards from reference tag molecules incorporated at hotspots,[28−31] and the calibrated SERS signals can more accurately reflect the actual biomolecule concentration. However, the tag molecule-based internal standards suffer significant limitations due to (i) poor photostability under laser excitation, (ii) spectral interference with Raman signatures of biomolecule matrices, and (iii) adsorption competition with biomolecules at hotspots, especially detrimental to chronic living cell measurements and analysis. To overcome the aforementioned limitations of tag molecule-based SERS calibration, our group has recently demonstrated that plasmon-enhanced electronic Raman scattering (ERS) signals from metal nanostructures can serve as a new internal standard to allow both spatial and temporal calibration of SERS signals for quantitative analysis of analyte molecules.[27]

Herein, we propose that plasmonically calibrated label-free SERS can achieve an improved multivariate analysis of living biological systems by increasing the correlations of Raman fingerprint features with molecular concentration profiles of complex biochemical matrices at hotspots. For the first time, we experimentally manifest the effectiveness of the ERS-based SERS calibration methodology in enhancing the supervised learning classification of living cell SERS spectra for cancer subtyping and drug efficacy testing. By exploiting biocompatible Au-based plasmonic nanolaminate substrates with dense uniform hotspot arrays, we can successfully achieve the cell culture on the SERS substrates to conduct SERS measurements of living cells under near-infrared (NIR) laser excitation at 785 nm. To assess the effects of ERS-based SERS calibration on the living cell multivariate analysis performance, we use two supervised learning approaches (e.g., PCA-LDA and PLS-DA) for the classification of SERS spectra from four biologically well-studied living breast cell lines, including a nonmalignant breast normal cell line (MCF-10A), a moderately malignant breast cancer cell line (MCF-7), and two highly malignant breast cancer cell lines (MDA-MB-231 and HCC-1806). From the side-by-side comparison of statistical analysis results from ERS-calibrated and noncalibrated SERS datasets, we show that the ERS calibration method can improve the statistical classification accuracy in cancer subtyping using extracellular SERS features from different living cells. We further investigate the effects of the ERS-based SERS calibration on the multivariate analysis of living cancer cells in response to an anticancer drug, paclitaxel (PTX), at different dosages. To assess the ERS calibration's contribution to the statistical classification of living cancer cells' drug responses, we employ two different breast cancer cell lines (MDA-MB-231 and HCC-1806) that have different half-maximal inhibitory concentration (IC_{50}) values to the same anticancer drug (PTX). Compared to noncalibrated SERS datasets, ERS-calibrated SERS datasets can increase classification accuracy for resolving different cancer cells' dosage-dependent responses, highly desirable for label-free living cell studies in drug efficacy testing. Therefore, we envision that the plasmonic ERS-based calibration method can significantly boost the multivariate analysis performance in label-free SERS measurements of living biological systems and other complex biochemical matrices.

EXPERIMENTAL SECTION

Cell Culture and Paclitaxel Treatment. MDA-MB-231 (American Type Culture Collection, ATCC) was grown in F12:DMEM (Dulbecco's Modified Eagle Medium, Lonza, Basel, Switzerland) with 4 mM glutamine, 10% fetal bovine serum (FBS), and penicillin−streptomycin (100 units per mL). HCC-1806 (ATCC) was grown in an ATCC-formulated RPMI-1640 medium (Roswell Park Memorial Institute 1640 medium, enriched with L-glutamine, 4-(2-hydroxyethyl)-1-piperazineethanesulfonic acid (HEPES), and sodium pyruvate, ATCC 30-2001) with 10% FBS and 1% PenStrep (100 units/mL penicillium and 100 μg/mL streptomycin). MCF-7 cells (ATCC) were grown in EMEM with 10% FBS and 2× L-glutamine. MCF-10A cells (Lombardi Comprehensive Cancer Center, Georgetown University in Washington, D.C.) were grown in F12:DMEM with penicillin−streptomycin (100 units/mL), 20 ng/mL epidermal growth factor (EGF), 2.5 mM L-glutamine, 10 μg/mL insulin, 0.1 μg/mL cholera toxin, 0.5 μg/mL hydrocortisone, and 5% horse serum. All cells were grown in T-25 cm^2 culture flasks (Corning, NY) at 37 °C in a 5% CO_2 in air atmosphere. Cells were then trypsinized and seeded on nanolaminated SERS substrates. Paclitaxel (Sigma Aldrich) was diluted in dimethyl-sulfoxide (DMSO, ATCC) with a concentration of 1.5, 5, and 15 μM for three different drug treatment concentrations. The solutions were mixed with 1 mL of the culture medium for the final drug concentrations of 1.5, 5, and 15 nM. The culture medium for the control group contains the same DMSO concentration as the drug treatment medium. The control group was prepared by adding 1 μL of DMSO in 1 mL of the culture medium. Once the cells were grown to ≈ 70% confluence, the medium was replaced by the new medium with paclitaxel.

https://dx.doi.org/10.1021/acs.analchem.0c05206
Anal. Chem. 2021, 93, 4601−4610

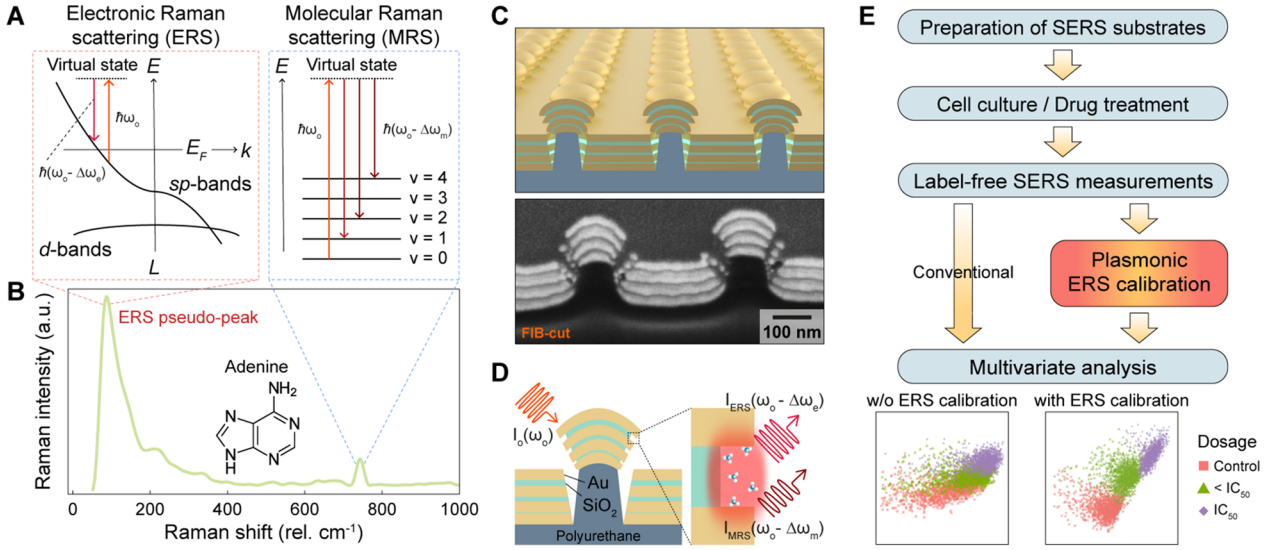

Figure 1. ERS signals in SERS measurements and ERS calibration for label-free living cell SERS biostatistical analysis. (A) Energy diagram illustration of the ERS process (left) and the MRS process (right). (B) Representative SERS spectrum using adenine molecules, showing the ERS pseudo-peak and MRS signals. (C) Schematic illustration of nanolaminated SERS substrates (top) and corresponding cross-sectional scanning electron microscope (SEM) image achieved by FIB milling. (D) Schematic illustration of the ERS and MRS processes at plasmonic hotspots in a unit cell of nanolaminated SERS substrates. (E) Flow diagram of the major steps for ERS calibration-enabled improved multivariate analysis of living cell SERS.

Raman Measurement. We used a confocal Raman microscope (Alpha 300 RSA+, WITec, Germany) for SERS measurements under laser excitation at 785 nm (Toptica Photonics, Germany) via a 20× objective (NA = 0.4). For 2D Raman mapping of living cells, a 20× water immersion objective (NA = 0.5) was used with 5 mW laser power and 20 ms integration time per pixel over a 100 μm × 100 μm area. Before the measurement, the instrumental calibration was verified by the silicon peak at 520 cm^{-1}. All measurements were conducted in the backscattering geometric configuration at room temperature. A long-pass filter blocks elastically scattered radiation at the wavelength corresponding to the laser line (Rayleigh scattering). Simultaneously, the rest of the collected light was guided through a multimode fiber (100 μm core diameter), acting as the pinhole for a confocal microscope, to a spectrometer (UHTS 300, WITec, Germany). The backscatter photons were dispersed with a 300 groove mm^{-1} (750 nm blaze grating) and detected by a CCD camera (DU-401A BR-DD-352, Andor Technology, UK), which was thermoelectrically cooled and maintained at −60 °C.

Data Processing and Multivariate Analysis. Cosmic ray removal was conducted by instrument-embedded software (Project v4.1, WITec). Smoothing interpolation and data truncation were carried out with the R package hyperSpec. PCA and peak picking were done with the R packages ChemoSpec and MALDIquant, respectively. LDA and PLS-DA were performed using the R packages of MASS and mixOmics, respectively.

RESULTS AND DISCUSSION

Unlike molecular Raman scattering (MRS) signals from the molecule's vibrational modes to exhibit as discrete narrow emission peaks (Figure 1A-right), the ERS signals originate from the inelastic light scattering of electrons in sp-bands of metal nanostructures (Figure 1A-left) and thus present as a source of continuum emission background in SERS measurements. Recent studies report that the ERS signals can be the dominant contribution to the SERS background of gold-based plasmonic nanostructures under NIR laser excitation.[32−34] Notably, the use of Au plasmonic nanosensors and the NIR excitation is highly desirable for SERS measurements of living biological systems. (1) Au is a biocompatible material. (2) NIR excitation can result in low autofluorescence, minimum phototoxicity, and deeper penetration depth in characterizing living biological samples. We have recently reported that both MRS and ERS processes follow the same $|E_{loc}/E_o|^4$ enhancements at plasmonic hotspots, where E_{loc} and E_o are the magnitudes of local and incident electric fields, respectively, and ERS signals can act as an internal standard to calibrate SERS signals, resulting in reduced spatial and temporal variations.[27] Plasmon-enhanced ERS intensity exponentially increases with the reduced Stokes-shifted frequency ($\Delta\omega_e$) toward the zero value because of its linear dependence on the electron−hole pair density, $n_{e-h}(\Delta\omega_e) = \left|\exp\left(-\frac{\hbar\Delta\omega_e}{k_B T}\right) - 1\right|^{-1}$, in metal nanostructures,[32−34] where $\hbar$ is the Planck constant, k_B is the Boltzmann constant, and T is the temperature. Therefore, in SERS measurements, by filtering Rayleigh scattering with a long-pass filter, a prominent ERS pseudo-peak (Figure 1B) can be generated as the SERS calibrator at the low-wavenumber range (<100 cm^{-1}). As derived in our previous work,[27] the ratio between MRS and ERS signals from the same plasmonic hotspots can be approximated as

$$\frac{I_{MRS}}{I_{ERS}} = \left|\frac{\varepsilon_M}{\varepsilon_I}\right|^4 \frac{\sigma_{MRS}(\omega_o, \Delta\omega_m)}{\sigma_{ERS}(\omega_o, \Delta\omega_e)} \frac{1}{|n_{e-h}(\Delta\omega_e) + 1|} \cdot r \cdot N$$

where ε_M and ε_I are the complex permittivity of the metal and the insulator, respectively, at the incident laser frequency ω_o, σ_{ERS} and σ_{MRS} are the effective cross sections for the ERS and MRS processes, respectively, $\Delta\omega_m$ is the Stokes-shifted frequency for the MRS process, r is the effective orientation coefficient of analyte molecules, and N is the molecular

https://dx.doi.org/10.1021/acs.analchem.0c05206
Anal. Chem. 2021, 93, 4601−4610

concentration. Apart from r and N, the other terms can be expressed as a material-based constant M. Therefore, the ratio between MRS and ERS signals can be further approximated as $I_{MRS}/I_{ERS} = M{\cdot}r{\cdot}N$. Compared to noncalibrated SERS signals (I_{MRS}), the ERS-calibrated SERS signals (I_{MRS}/I_{ERS}) are less affected by local field variations at hotspots and can more accurately reflect the molecular concentrations in complex biochemical matrices. Notably, the plasmonically enhanced ERS signals can serve as the internal SERS calibration standard for low-uniformity SERS substrates consisting of plasmonic nanoparticle aggregations and high-uniformity nanolaminate SERS substrates.[27]

Figure 1E shows a flow diagram to achieve ERS calibration for multivariate analysis of label-free living cell SERS. For the first step of "Preparation of SERS substrates," as shown in Figure 1C,D, we use nanolaminated SERS substrates consisting of vertically stacked hotspots with large and RI-insensitive SERS enhancement factors (EFs) (>10^7).[20,35] This RI-insensitive SERS property is due to the multiresonant optical property of vertically stacked metal−insulator−metal (MIM) nanostructures. For example, the RI of intracellular and extracellular components in cellular systems can vary from 1.30 to 1.60.[36,37] The integration of nanolaminated MIM nanostructures on vertical nanopillar arrays can promote the cellular engulfing activities and form an intimate nano-bio interface between cell membranes and plasmonic nano-antennas,[38−40] desirable for SERS profiling of biomolecules on cell membranes. The molding technique of soft lithography provides good fabrication scalability allowing mass production of large-area (≈16 cm^2) uniform hotspot arrays with cost-effectiveness, beneficial to biological applications. For the second step of "Cell culture and drug treatment," we directly cultured different breast normal and cancer cells on the nanolaminated SERS substrates. To conduct the drug efficacy study, we delivered an anticancer drug to living cancer cells with specific dosages, including IC_{50}, followed by the third step of "Label-free SERS measurements." Finally, we demonstrate multivariate analysis for living cell subtype classification and drug efficacy assessment with systematic comparisons between before and after ERS calibration.

To demonstrate ERS calibration's effectiveness to allow quantitative SERS analysis of biomolecules, we performed label-free SERS measurements of adenine molecules in phosphate-buffered-saline (PBS) solution with different concentrations from 1 to 100 μM (Figure 2). The samples were immersed in the solutions, and we acquired 2D Raman mapping results over a 100 μm × 100 μm area containing 20 pixels × 20 pixels. Figure 2A shows a Raman spectrum of 60 μM adenine without ERS calibration and the corresponding 2D Raman image (inset) using a peak at 745 cm^{-1} (ring-breathing mode). We can observe a large standard deviation (SD) (gray region) and, accordingly, a large coefficient of variation (CV) value of 26%. On the other hand, in Figure 2B, the ERS-calibrated SERS signals show a much smaller SD with 12% CV, and the 2D Raman image shows a more uniform intensity distribution over the large area with reduced spatial variations. Original spectra of before and after ERS calibration are available in Figure S1. To evaluate ERS calibration improvement for quantitative analysis, we plotted the working curve from 1 to 100 μM using the peak at 745 cm^{-1} (Figure 2C,D). By ERS calibration, we observe that the calibrated SERS signals more smoothly fit the Langmuir adsorption curve with reduced CV values for the equilibrium constant, K_T, from

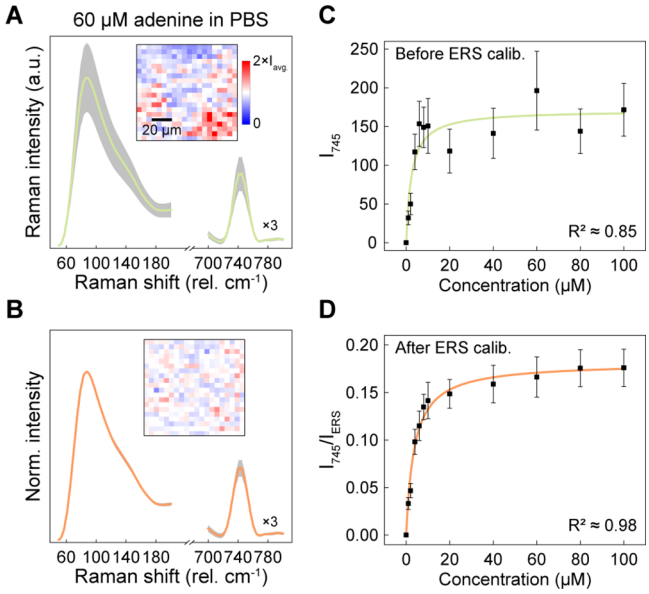

Figure 2. ERS calibration for quantitative SERS analysis of solution-based adenine molecules. (A,B) Averaged SERS spectrum of 60 μM adenine solution with SD (gray shaded regions) (A) before and (B) after ERS calibration. The MRS region between 700 and 800 cm^{-1} is multiplied by three for clarity. (inset) Corresponding 2D Raman images over a 100 μm × 100 μm area. (C,D) Working curves of adenine molecules in PBS solution with different concentrations from 1 to 100 μM using the adenine peak at 745 cm^{-1} (C) before and (D) after ERS calibration.

37.6% (4.1 × 10^5 ± 1.54 × 10^5 L/mol) to 11.1% (2.7 × 10^5 ± 0.30 × 10^5 L/mol). The SDs of all concentrations were significantly reduced with shorter error bars, and R^2 values increased from 0.85 to 0.98. We calculated the surface coverage (θ) of adenine molecules (Figure S2) with the equation expressed as $\theta = \frac{K_T \times C}{(1 + K_T \times C)}$, where C is the adenine concentration. After ERS calibration, the scatters show a better linear fitting with an improved convergence and increased R^2 values from 0.972 to 0.997.

To examine the effectiveness of ERS calibration on label-free SERS analysis of living cells, we conducted 2D Raman mapping measurements of breast normal and cancer cells cultured on the nanolaminated SERS substrates and compared the SERS profiles before and after ERS calibration (Figure 3). Here, we selected four different human breast normal and cancer cell lines with different degrees of malignancy covering a broad range of breast tumor types, including nonmalignant breast normal cells (MCF-10A), moderately malignant breast cancer cells (MCF-7), and highly malignant breast cancer cells (MDA-MB-231 and HCC-1806). Both MDA-MB-231 and HCC-1806 are triple-negative breast cancer (TNBC) cells, which lack targetable receptors of progesterone (PR), estrogen (ER), and human epidermal growth factor receptor 2 (HER2). TNBC cells, therefore, have been reported to have a significantly higher risk of recurrence and the worst survival rates among subtypes of breast tumors.[41]

Figure 3A shows the scheme of the experimental setup. A confocal Raman microscope under backscattering configuration equipped with a 20× water immersion objective (NA = 0.5) and 785 nm laser excitation was used for mapping label-free SERS spectra of living cells. To minimize time-dependent effects on the living cell SERS spectra due to the dynamic

https://dx.doi.org/10.1021/acs.analchem.0c05206
Anal. Chem. 2021, 93, 4601−4610

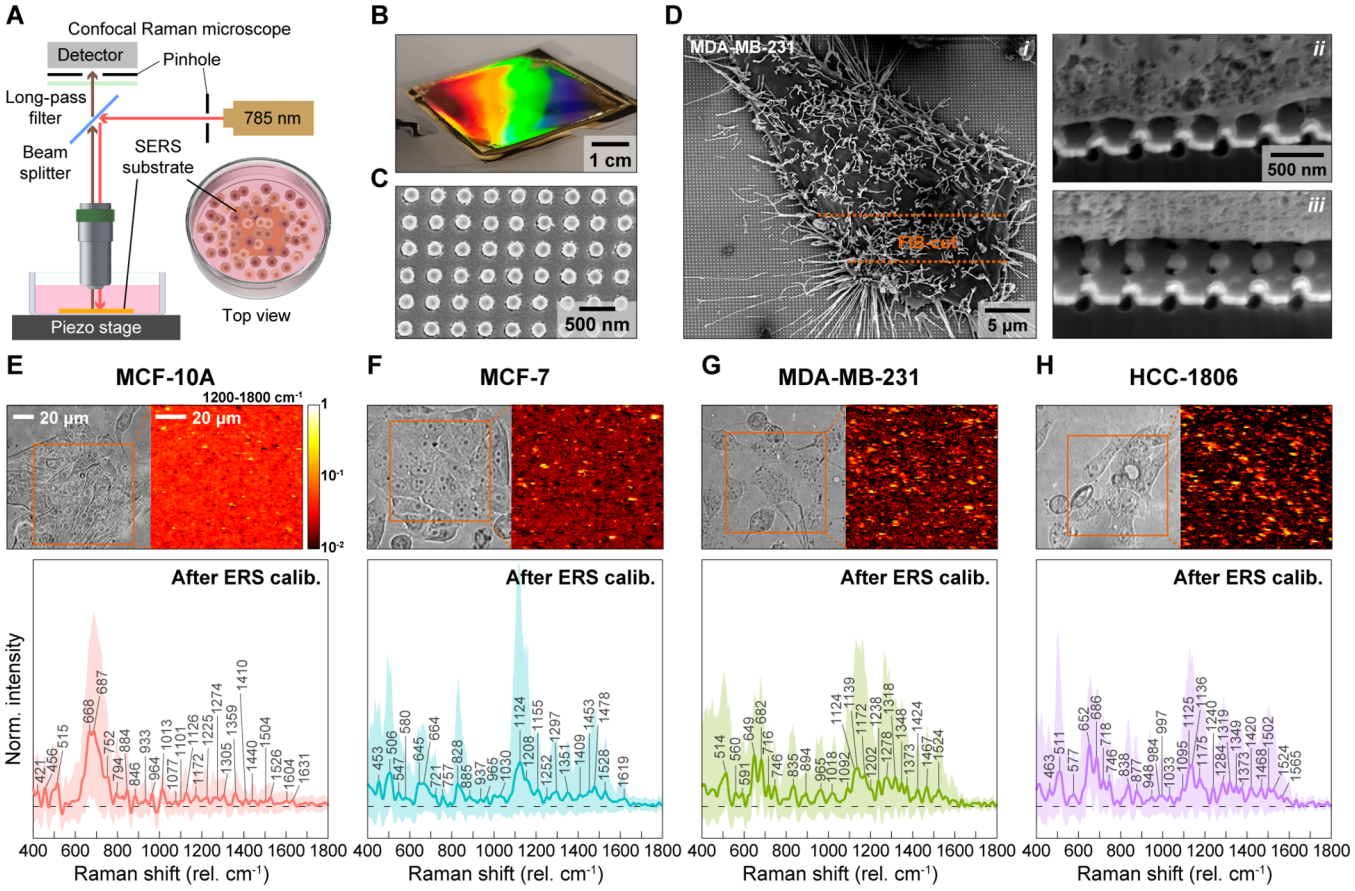

Figure 3. 2D label-free SERS measurements of living breast normal and cancer cells cultured on the nanolaminated SERS substrates. (A) Schematic illustration of the experimental setup for label-free living cell SERS measurements. (B) Photograph and (C) SEM image of the nanolaminated SERS substrates. (D) (i) Top-view and (ii,iii) cross-sectional view of SEM images of MDA-MB-231 cultured on the nanolaminated SERS substrates. (E–H) Bright-field images (top left), 2D Raman images (top right), and averaged SERS spectra of living cells after ERS calibration (bottom) for (E) MCF-10A, (F) MCF-7, (G) MDA-MB-231, and (H) HCC-1806. 2D Raman images were plotted using the integrated Raman signals of the protein-related region (1200–1800 cm^{-1}). The shaded regions in the averaged spectra are the 5th and 95th quartiles.

metabolic processes and stress responses to the nutrient-free environments, we restricted SERS mapping measurements within 2 h without changing culture media with other solutions.[3] As shown in Figure 3B,C of the representative photograph and SEM image, nanolaminated SERS substrates have good nanoscale uniformity. A large-area top-view SEM image is shown in Figure S3. Figure 3D shows top-view and cross-sectional SEM images of MDA-MB-231 cultured on the nanolaminated SERS substrates. The membrane surface feature of the cultured MDA-MB-231 agrees with a previously reported study that such cancer cells reveal brush structures, consisting of microvilli and cilia with different lengths (Figure 3D-i).[42] Furthermore, previous reports show that vertical nanopillar structures can induce spontaneous cell engulfment,[38−40] and we expect that a tight interface between the cell membrane and nanolaminated SERS substrates can improve SERS detection sensitivity. The focused ion beam (FIB)-milled SEM image in Figure 3D-ii shows that a clear nano-bio interface was formed between them, allowing direct label-free SERS measurements of cell membrane components for living cells. However, as shown in Figure 3D-iii, some nanoantennas do not meet the cell membrane but may still detect extracellular biomolecules in their local microenvironments, such as secreted metabolites and exosomes.[43]

Figure 3E–H shows field images, 2D images of ERS-calibrated SERS signals, and averaged Raman spectra after ERS calibration of four different living breast cells. The 2D Raman images were acquired from a 100 μm × 100 μm area containing 10,000 pixels, which can accommodate a group of cells. The protein-relevant range (from 1200 to 1800 cm^{-1}) was used for 2D Raman maps. Enabled by high SERS EFs (>10^7) of the nanolaminated SERS substrates, we used a short integration time (20 ms) to collect Raman spectra with proper signal-to-noise ratios. In this way, each measurement for a Raman 2D mapping image over the large area takes only 3–5 min. Compared to conventional Raman imaging, rapid SERS spectroscopic imaging is incredibly valuable for bioanalysis of living cells by minimizing temporal deviations of molecular fingerprint information between different pixels in 2D Raman images due to dynamic cellular processes. For example, we observed that cancer cells sometimes underwent quick cell mitosis within 30–60 min (not shown).

By comparing 2D Raman images among different cells (the top row in Figure 3E–H), we can notice that the breast normal MCF-10A cells exhibit a more uniform signal distribution with brighter pixels than the three other types of cancer cells, which reflects the inherent cellular property of MCF-10A that forms an epithelial-like compact morphology.[44] Remarkably, despite the excellent hotspot uniformity of the nanolaminated SERS

https://dx.doi.org/10.1021/acs.analchem.0c05206
Anal. Chem. 2021, 93, 4601−4610

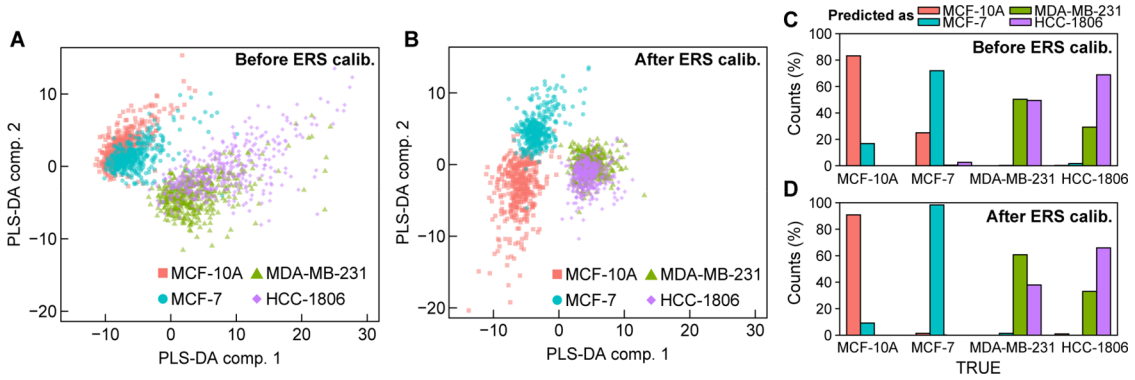

Figure 4. Improved SERS multivariate analysis by ERS calibration for subtype classification of living breast normal and cancer cells. (A,B) PLS-DA scatter plots of four different living breast normal and cancer cells (A) before and (B) after ERS calibration. (C,D) Histograms of the LOOCV confusion matrix (C) before and (D) after ERS calibration.

substrate, there is no direct spatial correlation of cell morphologies in bright-field images with 2D Raman images for different living cells, which reflects the heterogeneous, dynamic, and stochastic adsorption processes of different biomolecules at plasmonic hotspots distributed over the SERS substrates.[3,15] The middle and bottom rows in Figure 3E−H, respectively, show the average SERS spectra after ERS calibration with 5th and 95th quartiles (shaded regions) from four living breast cells. The 2D Raman images and SERS spectra before ERS calibration are shown in Figure S4. These spectral results highlight the following critical points. First, the SERS spectra measured from all living cells show significant pixel-to-pixel variations due to the spatial heterogeneity of SERS signals from cellular biomolecules at plasmonic hotspots.[3,15,45] Second, all living cells exhibit rich fingerprint profiles over a wide wavenumber range between 400 and 1700 cm^{-1}. Third, although we can observe subtle differences between spectral profiles before (Figure S4) and after ERS calibration, it is difficult to evaluate whether ERS calibration improved the quality of living cell SERS spectra. Therefore, these observations justify using statistical approaches for analyzing the subtle differences of complex label-free SERS spectroscopic imaging data from different types of living cells.

Significantly, the average SERS spectra (Figure 3E−H) can reveal that the measured SERS signals originate from viable living cells. First, the absence of broad carbon-based D (1350 cm^{-1}) and G (1580 cm^{-1}) bands reflects that the laser excitation conditions did not induce the photothermal graphitization of biomaterials, which can be deposited on hotspots and can mask weak SERS signals. Second, the absence of the phosphatidylserine(s) Raman signals (524, 733, and 787 cm^{-1}) from SERS hotspots in extracellular regions suggests that the measured cells are living since phosphatidylserine(s) is no longer restricted to face the inner leaflet of the plasma membrane when cells undergo apoptosis.[46] Third, the absence of Raman "death bands" of benzene ring stretching (1000 cm^{-1}) and N−H out-of-plane bending (1585 cm^{-1}) modes also reflects a healthy state of the measured cells.[47] Finally, the DNA backbone (1125 cm^{-1}) peak appearance along with lack of adenine ring-breathing mode (735 cm^{-1}) indicates a nondenaturalized configuration of DNA from living cells.[48]

As shown in Figure 3E−H, all cancer cells reveal higher SERS intensities with more peaks in the lipid-relevant ranges (780 to 890 cm^{-1} and 1400 to 1550 cm^{-1}),[49] reflecting increased lipid-related components by the amplified synthesis of fatty acid and phospholipids.[50,51] Similarly, all cancer cells show weak or almost no collagen peaks (815 and 852 cm^{-1}), indicating a reduced collagen feature in cancer cells.[52] In addition, TNBC cells exhibit weak proline (855 cm^{-1}) and phospholipid (1454 cm^{-1}) intensities.[53] A common thing for the three different breast cancer cells is that they all show strong phenylalanine (621, 645, and 1170 cm^{-1}), tryptophan (879, 1208, and 1348 cm^{-1}), and tyrosine (825, 1164, and 1178 cm^{-1}) peaks compared to nonmalignant cells, suggesting the increased aromatic amino acid-rich proteins on their surfaces.[51,53] Remarkably, we can observe large variations of amide III bands (1200 to 1350 cm^{-1})[54] from the MCF-7 cancer cells with moderate malignancy as well as from the MDA-MB-231 and HCC-1806 TNBC cells with high malignancy. The observation of large amide III band variations can be associated with the disordered proteins with the beta-sheet conformation, indicating a more considerable degree of protein structural instability, i.e., less rigid and stable, consistent with the higher deformability of cancer cells.[55]

Despite the significance, the direct SERS bioanalysis of living cells by the spectroscopic fingerprint features has significant limitations, including the masking of crucial information from low-concentration biomolecules and spectral interference between different biomolecule ensembles.[15,45] Therefore, multivariate statistical methods can play a crucial role in analyzing inhomogeneous Raman spectroscopic data from label-free biological samples.[3] This study used PLS-DA[56] as a supervised classification machine learning method to maximize interclass variance among different types of cells. To investigate the effects of ERS calibration on the statistical SERS bioanalysis performance for living cells, we performed PLS-DA for the SERS dataset before and after ERS calibration (Figure 4). Before ERS calibration, PLS-DA scatter plots in Figure 4A show two groups of overlapped scatters for (1) breast normal MCF-10A cells and moderately malignant MCF-7 cancer cells and for (2) highly malignant MDA-MB-231 and HCC-1806 TNBC cells. After ERS calibration (Figure 4B), the scatters of MCF-10A cells can be separated from those of MCF-7 cells, while the scatters of MDA-MB-231 and HCC-1806 TNBC cells still overlap due to their similar surface protein expressions.[41,57] Therefore, the ERS calibration process can improve the statistical SERS bioanalysis to classify between different cell lines, suggesting that achieving a more accurate scaling of Raman fingerprint signature intensities in the measured SERS spectra from different pixels can play a positive role in the statistical analysis of biological samples.

https://dx.doi.org/10.1021/acs.analchem.0c05206
Anal. Chem. 2021, 93, 4601−4610

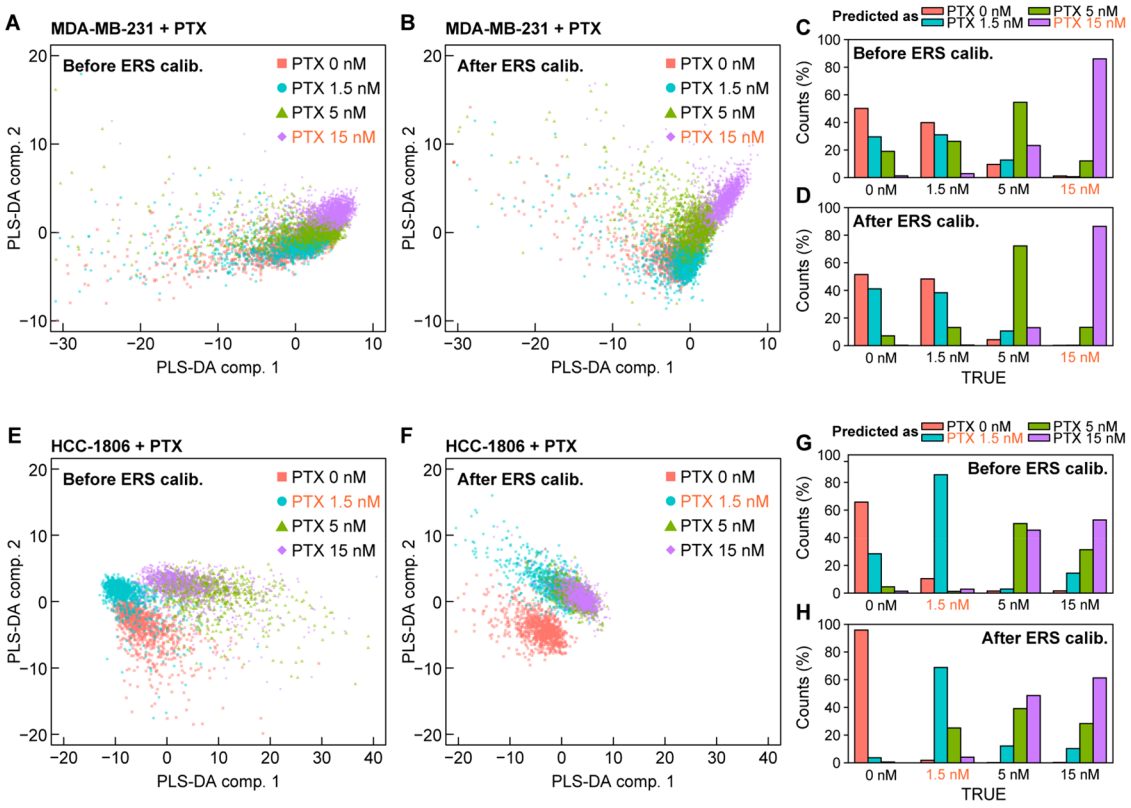

Figure 5. Improved SERS multivariate analysis by ERS calibration for the dosage-dependent drug efficacy study for TNBC cells. (A,B) PLS-DA scatter plots of MDA-MB-231 treated by different PTX dosages (A) before and (B) after ERS calibration. (C,D) Histograms of the LOOCV confusion matrix of the MDA-MB-231 dataset (C) before and (D) after ERS calibration. (E,F) PLS-DA scatter plots of HCC-1806 treated by different PTX dosages (E) before and (F) after ERS calibration. (G,H) Histograms of the LOOCV confusion matrix of the HCC-1806 dataset (C) before and (D) after ERS calibration. IC_{50} of PTX for each TNBC is labeled with an orange color.

After ERS calibration, we can separate human breast cell lines into three different groups based on the degree of malignancy: (1) nonmalignant (MCF-10A), (2) moderately malignant (MCF-7), and (3) highly malignant (MDA-MB-231 and HCC-1806 TNBC cells). Subtype classification among different breast cancer cells by the degree of malignancy can be achieved due to significant molecular differences in transmembrane proteins between luminal A subtype (MCF-7) and TNBC cells,[58] and in vimentin expression, one of the cytoskeletal components in charge of retaining cell integrity.[59] MDA-MB-231 express vimentin, which makes it a more mesenchymal type than HCC-1806.[57] Vimentin is typically attached to the nucleus, endoplasmic reticulum, and mitochondria.[60] To test the generality of ERS calibration for improving statistical bioanalysis, we have also used a combination of PCA and LDA to process the same SERS dataset with and without ERS calibration, showing very similar results as the PLS-DA method (Figure S5).

PLS-DA prediction abilities with and without ERS calibration can be assessed in an unbiased manner using the leave-one-out cross-validation (LOOCV) approach, and Figure 4C,D shows the confusion matrix results in histograms. Table S1 shows the confusion matrices of the raw numbers of spectra. Here, we use LOOCV to assume that each spectrum independently represents a specific cell type among four different cell lines. With ERS calibration, the PLS-DA prediction accuracy increases from 71 to 98% for MCF-7 and increases from 83 to 91% for MCF-10A. In contrast, after ERS calibration, MDA-MB-231 shows a prediction accuracy slightly improved from 50 to 60%, and HCC-1806 maintains a prediction accuracy around 65%, indicating that the two TNBC cell lines possess similar molecular Raman fingerprint profiles of extracellular and membrane proteins in SERS measurements.

Given the ERS calibration-enabled improvement in statistical classification between normal breast cells and different subtypes of breast cancer cells, we further investigated ERS calibration effects on statistical bioanalysis performance in drug testing for living cancer cells. Based on the previous studies,[61−63] we chose to use PTX as a potent anticancer drug, which can stabilize microtubules and prevent cancer cell division, to treat the two highly malignant TNBC cells (i.e., MDA-MB-231 and HCC-1806). As reported in a previous study,[64] the IC_{50} value for PTX to MDA-MB-231 cells is 12−15 nM, while the IC_{50} value for PTX to HCC-1806 cells is 0.8−2.0 nM. It is crucial to determine the IC_{50} values for a specific anticancer drug to a specific cancer cell, helping refine a proper chemotherapy procedure in cancer treatment. With preknowledge of the different IC_{50} values for PTX to MDA-MB-231 and HCC-1806 cells, we can choose a series of PTX dosages to examine dosage-dependent drug effects on both cells in statistical SERS bioanalysis. We conducted 2D SERS mapping measurements of living MDA-MB-231 and HCC-1806 cells under different PTX dosages and compared SERS statistical bioanalysis performance with and without ERS calibration. Specifically, the cells treated with 0 nM PTX in dimethyl-sulfoxide (DMSO) serve as a control. To confirm that acquired SERS signals originate from living cells rather

https://dx.doi.org/10.1021/acs.analchem.0c05206
Anal. Chem. 2021, 93, 4601−4610

than chemical components of culture media or drugs, we conducted SERS measurements of bare culture media with and without PTX. As expected, due to the relatively low concentration of chemicals, we did not observe any distinct Raman peaks (Figure S6).

Figure 5A,B shows PLS-DA scatter plots measured from living MDA-MB-231 cells treated with different PTX dosages before and after ERS calibration, respectively. Before ERS calibration (Figure 5A), the scatters of the low-dosage group (1.5 nM) considerably overlap with those of the control group (0 nM), while the scatters of the high-dosage group (IC_{50}, 15 nM) are separated from the control group. The scatters of the middle-dosage group (5 nM) are distributed between the low- and the high-dosage groups with apparent overlaps. After ERS calibration (Figure 5B), the separations among scatters of the low (1.5 nM)-, the middle (5 nM)-, and the high (15 nM)-dosage groups are more pronounced, indicating improved molecular fingerprint profiling and bioanalysis of living cancer cell status upon drug perturbations with different dosages. On the other side, the scatters of the control (0 nM) group and the low-dosage (1.5 nM) group still have a significant overlap after ERS calibration. This observation suggests that the PTX treatment with one order of magnitude lower dosage (1.5 nM) than IC_{50} (15 nM) is not enough to elicit significant changes of SERS-measured molecular profiles to statistically distinguish the drug effects on MDA-MB-231 cells compared to the control group (0 nM).

By comparing LOOCV confusion matrix histograms for PLS-DA results before (Figure 5C) and after (Figure 5D) ERS calibration, we can further quantify the prediction accuracy improvement in statistical SERS bioanalysis. After ERS calibration, the prediction accuracy rate for the middle-dosage (5 nM) group increases from 54 to 72%, while the prediction accuracy rate for the high-dosage IC_{50} group (15 nM) remains around 86%. For the nearly indistinguishable control (0 nM) and low-dosage (1.5 nM) groups, the prediction inaccuracy rates assigned to the 5 and 15 nM groups are reduced significantly from 20 to 7% and from 29 to 13%, respectively. These observations imply that there may be a threshold PTX drug dosage value below 15 nM (IC_{50}) and above 5 and 15 nM to induce sufficient changes in SERS-measured molecular profiles to distinguish the drug effects on MDA-MB-231 cells. Future research can exploit ERS-calibrated SERS bioanalysis to investigate dynamic responses of living cells upon drug perturbations with different dosage levels.

Figure 5E,F shows PLS-DA scatter plots measured from living HCC-1806 cells with different PTX dosages before and after ERS calibration, respectively. Before ERS calibration, the scatters of the low-dosage group (IC_{50}, 1.5 nM) exhibit substantial overlap with the control group (0 nM), while the scatters of the middle-dosage (5 nM) and the high-dosage (15 nM) groups overlap each other with separation from the control group (0 nM) and the low-dosage IC_{50} (1.5 nM) group. Remarkably, after ERS calibration, the scatters of the control group (0 nM) can completely separate from the three PTX-treated groups (1.5, 5, and 15 nM). Among the three PTX-treated groups, after ERS calibration, we can observe a gradual convergence of the scatter distributions evolving from the low-dosage group (1.5 nM) to the higher-dosage groups (5 and 15 nM) with accompanying reduced scatter distribution areas.

As shown in Figure 5G,H, after ERS calibration, the control group's (0 nM) prediction accuracy rate was significantly improved from 66 to 96% with reduced overlaps of its scatters with the low-dosage IC_{50} (1.5 nM) group. In comparison, the prediction accuracy rate for the low-dosage IC_{50} (1.5 nM) group decreases from 85 to 69% due to increased overlaps of its scatters with the middle-dosage (5 nM) and the high-dosage (15 nM) groups. The prediction accuracy rates for the middle-dosage (5 nM) and the high-dosage (15 nM) groups do not change much after ERS calibration. In Figure 5F, the observed converging of the scatter distributions toward the high-dosage group (15 nM) is due to the drug saturation effects because the cancer cells treated with the drug dosage above IC_{50} will have similar biological behaviors with stopped mitosis by binding PTX molecules with most of the microtubules.[61−63] In the PLS-DA scatter plot after ERS calibration (Figure 5F), the scatters of the low-dosage IC_{50} (1.5 nM) group have a more extensive distribution area than the higher-dosage groups (5 and 15 nM). These observations reveal that compared to the cancer cells treated by higher dosage experiencing drug saturation effects, the population of IC_{50} cancer cells can have a broader range of cellular biochemical states associated with the stochastic drug perturbation of cell cycle (mitotic-arrest) and apoptosis processes.[62,63] Therefore, with ERS calibration, SERS molecular profiles of drug-treated living cells can allow a more accurate biostatistical analysis to distinguish dosage-dependent drug responses of living cancer cells. Compared to conventional immune-staining assays widely used for in vitro drug efficacy assessment, ERS-calibrated SERS bioanalysis can allow noninvasive, label-free, and real-time monitoring of living cells to investigate dynamic cellular behaviors in response to perturbations from drugs or other physical/chemical stimuli.

CONCLUSIONS

In summary, we show that ERS calibration can improve the quantitative analysis of adenine molecules in solutions, resulting in a smoother fitting with the Langmuir adsorption curve. In particular, we demonstrate that applying ERS calibration to label-free living cell SERS measurements can improve the classification accuracy of supervised learning approaches in subtyping breast normal and cancer cells with different degrees of malignancy. Furthermore, ERS calibration can enhance the supervised learning classification for dosage-dependent anticancer drug responses of living TNBC cells. By avoiding using Raman tags, the ERS calibration approach demonstrated in this work has several crucial advantages, such as no adsorption competition and no spectral interference with target analytes and excellent photochemical and photothermal stability. Therefore, the plasmonic ERS-based calibration method can enhance the multivariate analysis of label-free SERS datasets from living biological systems and open new opportunities in biology and medicine, including spatiotemporal monitoring and analysis of biological processes in living cells and cellular networks, rapid real-time drug reaction assessment of living normal and cancer cells for personalized medicine, and long-term in vivo monitoring of disease states with implantable SERS devices.

ASSOCIATED CONTENT

Supporting Information

The Supporting Information is available free of charge at https://pubs.acs.org/doi/10.1021/acs.analchem.0c05206.

https://dx.doi.org/10.1021/acs.analchem.0c05206
Anal. Chem. 2021, 93, 4601−4610

Fabrication of nanolaminated SERS substrates, FIB-SEM characterization, original SERS spectra of adenine molecules before and after ERS calibration, calculated surface coverage before and after ERS calibration, top-view SEM image of nanolaminated SERS substrates, 2D Raman images and SERS spectra of different living cells before ERS calibration, PCA-LDA scatter plots for four different breast cells for subtype classification, SERS spectra of the culture media with and without PTX, and confusion matrix for PLS-DA LOOCV results with raw numbers of datasets (PDF)

AUTHOR INFORMATION

Corresponding Author

Wei Zhou − *Department of Electrical and Computer Engineering, Virginia Tech, Blacksburg, Virginia 24061, United States;* orcid.org/0000-0002-5257-3885; Email: wzh@vt.edu

Authors

Wonil Nam − *Department of Electrical and Computer Engineering, Virginia Tech, Blacksburg, Virginia 24061, United States;* orcid.org/0000-0002-7804-3049

Xiang Ren − *Department of Electrical and Computer Engineering, Virginia Tech, Blacksburg, Virginia 24061, United States*

Inyoung Kim − *Department of Statistics, Virginia Tech, Blacksburg, Virginia 24061, United States*

Jeannine Strobl − *Department of Electrical and Computer Engineering, Virginia Tech, Blacksburg, Virginia 24061, United States*

Masoud Agah − *Department of Electrical and Computer Engineering, Virginia Tech, Blacksburg, Virginia 24061, United States*

Complete contact information is available at: https://pubs.acs.org/10.1021/acs.analchem.0c05206

Notes

The authors declare no competing financial interest.

ACKNOWLEDGMENTS

This work was supported by the Air Force Office of Scientific Research (AFOSR) Young Investigator Award FA9550-18-1-0328 and the National Cancer Institute (NCI) R21CA210216.

REFERENCES

(1) Kneipp, J.; Kneipp, H.; Kneipp, K. *Chem. Soc. Rev.* **2008**, *37*, 1052−1060.
(2) Cialla-May, D.; Zheng, X. S.; Weber, K.; Popp, J. *Chem. Soc. Rev.* **2017**, *46*, 3945−3961.
(3) Zong, C.; Xu, M.; Xu, L. J.; Wei, T.; Ma, X.; Zheng, X. S.; Hu, R.; Ren, B. *Chem. Rev.* **2018**, *118*, 4946−4980.
(4) Heck, A. J. R. *Nat. Methods* **2008**, *5*, 927−933.
(5) Dunn, W. B.; Broadhurst, D. I.; Atherton, H. J.; Goodacre, R.; Griffin, J. L. *Chem. Soc. Rev.* **2011**, *40*, 387−426.
(6) Zheng, X. S.; Jahn, I. J.; Weber, K.; Cialla-May, D.; Popp, J. *Spectrochim. Acta A Mol. Biomol. Spectrosc.* **2018**, *197*, 56−77.
(7) Garg, A.; Nam, W.; Zhou, W. *ACS Appl. Mater. Interfaces* **2020**, *12*, 56290−56299.
(8) Song, J.; Cheng, W.; Nie, M.; He, X.; Nam, W.; Cheng, J.; Zhou, W. *ACS Nano* **2020**, *14*, 9521−9531.
(9) Nie, S.; Emory, S. R. *Science* **1997**, *275*, 1102−1106.
(10) Bodelón, G.; Montes-García, V.; Costas, C.; Pérez-Juste, I.; Pérez-Juste, J.; Pastoriza-Santos, I.; Liz-Marzán, L. M. *ACS Nano* **2017**, *11*, 4631−4640.
(11) Matteini, P.; Cottat, M.; Tavanti, F.; Panfilova, E.; Scuderi, M.; Nicotra, G.; Menziani, M. C.; Khlebtsov, N.; de Angelis, M.; Pini, R. *ACS Nano* **2016**, *11*, 918−926.
(12) Morla-Folch, J.; Alvarez-Puebla, R. A.; Guerrini, L. *J. Phys. Chem. Lett.* **2016**, *7*, 3037−3041.
(13) Lussier, F.; Brulé, T.; Vishwakarma, M.; Das, T.; Spatz, J. P.; Masson, J.-F. *Nano Lett.* **2016**, *16*, 3866−3871.
(14) Kneipp, J. *ACS Nano* **2017**, *11*, 1136−1141.
(15) Kuku, G.; Altunbek, M.; Culha, M. *Anal. Chem.* **2017**, *89*, 11160−11166.
(16) Laing, S.; Jamieson, L. E.; Faulds, K.; Graham, D. *Nat. Rev. Chem.* **2017**, *1*, 0060.
(17) Aioub, M.; El-Sayed, M. A. *J. Am. Chem. Soc.* **2016**, *138*, 1258−1264.
(18) Kang, B.; Austin, L. A.; El-Sayed, M. A. *Nano Lett.* **2012**, *12*, 5369−5375.
(19) Huefner, A.; Kuan, W.-L.; Müller, K. H.; Skepper, J. N.; Barker, R. A.; Mahajan, S. *ACS Nano* **2015**, *10*, 307−316.
(20) Nam, W.; Ren, X.; Tali, S. A. S.; Ghassemi, P.; Kim, I.; Agah, M.; Zhou, W. *Nano Lett.* **2019**, *19*, 7273−7281.
(21) Ren, X.; Nam, W.; Ghassemi, P.; Strobl, J. S.; Kim, I.; Zhou, W.; Agah, M. *Microsyst. Nanoeng.* **2020**, *6*, 47.
(22) Caprettini, V.; Huang, J. A.; Moia, F.; Jacassi, A.; Gonano, C. A.; Maccaferri, N.; Capozza, R.; Dipalo, M.; De Angelis, F. *Adv. Sci.* **2018**, *5*, 1800560.
(23) El-Said, W. A.; Kim, S. U.; Choi, J.-W. *J. Mater. Chem. C* **2015**, *3*, 3848−3859.
(24) Morais, C. L. M.; Lima, K. M. G.; Singh, M.; Martin, F. L. *Nat. Protoc.* **2020**, *15*, 2143−2162.
(25) Ringnér, M. *Nat. Biotech.* **2008**, *26*, 303−304.
(26) Lussier, F.; Thibault, V.; Charron, B.; Wallace, G. Q.; Masson, J.-F. *TrAC, Trends Anal. Chem.* **2020**, *124*, 115796.
(27) Nam, W.; Zhao, Y.; Song, J.; Ali Safiabadi Tali, S.; Kang, S.; Zhu, W.; Lezec, H. J.; Agrawal, A.; Vikesland, P. J.; Zhou, W. *J. Phys. Chem. Lett.* **2020**, 9543−9551.
(28) Kleinman, S. L.; Ringe, E.; Valley, N.; Wustholz, K. L.; Phillips, E.; Scheidt, K. A.; Schatz, G. C.; Van Duyne, R. P. *J. Am. Chem. Soc.* **2011**, *133*, 4115−4122.
(29) Kasera, S.; Biedermann, F.; Baumberg, J. J.; Scherman, O. A.; Mahajan, S. *Nano Lett.* **2012**, *12*, 5924−5928.
(30) Shen, W.; Lin, X.; Jiang, C.; Li, C.; Lin, H.; Huang, J.; Wang, S.; Liu, G.; Yan, X.; Zhong, Q.; Ren, B. *Angew. Chem., Int. Ed.* **2015**, *54*, 7308−7312.
(31) Goodacre, R.; Graham, D.; Faulds, K. *TrAC, Trends Anal. Chem.* **2018**, *102*, 359−368.
(32) Carles, R.; Bayle, M.; Benzo, P.; Benassayag, G.; Bonafos, C.; Cacciato, G.; Privitera, V. *Phys. Rev. B* **2015**, *92*, 174302.
(33) Hugall, J. T.; Baumberg, J. J. *Nano Lett.* **2015**, *15*, 2600−2604.
(34) Mertens, J.; Kleemann, M. E.; Chikkaraddy, R.; Narang, P.; Baumberg, J. J. *Nano Lett.* **2017**, *17*, 2568−2574.
(35) Song, J.; Nam, W.; Zhou, W. *Adv. Mater. Technol.* **2019**, *4*, 1800689.
(36) Liu, P. Y.; Chin, L. K.; Ser, W.; Chen, H. F.; Hsieh, C. M.; Lee, C. H.; Sung, K. B.; Ayi, T. C.; Yap, P. H.; Liedberg, B.; Wang, K.; Bourouina, T.; Leprince-Wang, Y. *Lab Chip* **2016**, *16*, 634−644.
(37) Chatterjee, A.; Cerna Sanchez, J. A.; Yamauchi, T.; Taupin, V.; Couvrette, J.; Gorodetsky, A. A. *Nat. Commun.* **2020**, *11*, 2708.
(38) Hanson, L.; Zhao, W.; Lou, H. Y.; Lin, Z. C.; Lee, S. W.; Chowdary, P.; Cui, Y.; Cui, B. *Nat. Nanotechnol.* **2015**, *10*, 554−562.
(39) Zhao, W.; Hanson, L.; Lou, H. Y.; Akamatsu, M.; Chowdary, P. D.; Santoro, F.; Marks, J. R.; Grassart, A.; Drubin, D. G.; Cui, Y.; Cui, B. *Nat. Nanotechnol.* **2017**, *12*, 750−756.
(40) Lou, H.-Y.; Zhao, W.; Zeng, Y.; Cui, B. *Acc. Chem. Res.* **2018**, *51*, 1046−1053.

(41) Lehmann, B. D.; Bauer, J. A.; Chen, X.; Sanders, M. E.; Chakravarthy, A. B.; Shyr, Y.; Pietenpol, J. A. *J. Clin. Invest.* **2011**, *121*, 2750−2767.
(42) Iyer, S.; Gaikwad, R. M.; Subba-Rao, V.; Woodworth, C. D.; Sokolov, I. *Nat. Nanotechnol.* **2009**, *4*, 389−393.
(43) Gangoda, L.; Liem, M.; Ang, C. S.; Keerthikumar, S.; Adda, C. G.; Parker, B. S.; Mathivanan, S. *Proteomics* **2017**, *17*, 1600370.
(44) Maeda, M.; Johnson, K. R.; Wheelock, M. J. *J. Cell Sci.* **2005**, *118*, 873−887.
(45) Altschuler, S. J.; Wu, L. F. *Cell* **2010**, *141*, 559−563.
(46) Schlegel, R. A.; Williamson, P. *Cell. Death. Differ.* **2001**, *8*, 551−563.
(47) Austin, L. A.; Kang, B.; El-Sayed, M. A. *J. Am. Chem. Soc.* **2013**, *135*, 4688−4691.
(48) Kneipp, K.; Haka, A. S.; Kneipp, H.; Badizadegan, K.; Yoshizawa, N.; Boone, C.; Shafer-Peltier, K. E.; Motz, J. T.; Dasari, R. R.; Feld, M. S. *Appl. Spectrosc.* **2002**, *56*, 150−154.
(49) Czamara, K.; Majzner, K.; Pacia, M. Z.; Kochan, K.; Kaczor, A.; Baranska, M. *J. Raman Spectrosc.* **2015**, *46*, 4−20.
(50) Menendez, J. A.; Lupu, R. *Nat. Rev. Cancer* **2007**, *7*, 763−777.
(51) Bi, X.; Rexer, B.; Arteaga, C. L.; Guo, M.; Mahadevan-Jansen, A. *J. Biomed. Opt.* **2014**, *19*, No. 025001.
(52) Manciu, F. S.; Ciubuc, J. D.; Parra, K.; Manciu, M.; Bennet, K. E.; Valenzuela, P.; Sundin, E. M.; Durrer, W. G.; Reza, L.; Francia, G. *Technol. Cancer. Res. Treat* **2017**, *16*, 461−469.
(53) Movasaghi, Z.; Rehman, S.; Rehman, I. U. *Appl. Spectrosc. Rev.* **2007**, *42*, 493−541.
(54) Rygula, A.; Majzner, K.; Marzec, K. M.; Kaczor, A.; Pilarczyk, M.; Baranska, M. *J. Raman Spectrosc.* **2013**, *44*, 1061−1076.
(55) Swaminathan, V.; Mythreye, K.; O'Brien, E. T.; Berchuck, A.; Blobe, G. C.; Superfine, R. *Cancer Res.* **2011**, *71*, 5075−5080.
(56) Ballabio, D.; Consonni, V. *Anal. Methods* **2013**, *5*, 3790.
(57) Chavez, K. J.; Garimella, S. V.; Lipkowitz, S. *Breast. Dis.* **2010**, *32*, 35−48.
(58) Nieman, M. T.; Prudoff, R. S.; Johnson, K. R.; Wheelock, M. J. *J. Cell Biol.* **1999**, *147*, 631−644.
(59) Goldman, R. D.; Khuon, S.; Chou, Y. H.; Opal, P.; Steinert, P. M. *J. Cell Biol.* **1996**, *134*, 971−983.
(60) Katsumoto, T.; Mitsushima, A.; Kurimura, T. *Biol. Cell* **1990**, *68*, 139−146.
(61) Schiff, P. B.; Horwitz, S. B. *Proc. Natl. Acad. Sci.* **1980**, *77*, 1561−1565.
(62) Wang, T. H.; Wang, H. S.; Soong, Y. K. *Cancer* **2000**, *88*, 2619−2628.
(63) Weaver, B. A. *Mol. Biol. Cell* **2014**, *25*, 2677−2681.
(64) Volk-Draper, L. D.; Rajput, S.; Hall, K. L.; Wilber, A.; Rana, S. *Neoplasia* **2012**, *14*, 926−IN13.

https://dx.doi.org/10.1021/acs.analchem.0c05206
Anal. Chem. 2021, 93, 4601−4610